

Low-dark current 1.55 μm InAs quantum dash waveguide photodiodes

Yating Wan^{1, †, *}, Chen Shang^{2, †}, Jian Huang^{3, †}, Zhiyang Xie³, Aditya Jain⁴, Justin Norman², Baile Chen^{1,3}, Arthur C. Gossard^{1,2,4}, John E. Bowers^{1,2,4}

* Corresponding Author: yatingwan@ucsb.edu; cbl910@gmail.com

† These authors contributed equally to this work

¹ Institute for Energy Efficiency, University of California Santa Barbara, Santa Barbara, CA, USA, 93106

² Materials department, University of California Santa Barbara, Santa Barbara, CA, USA, 93106

³ School of Information Science and Technology, ShanghaiTech University, Shanghai 201210, China

⁴ Department of Electrical and Computer Engineering, University of California Santa Barbara, Santa Barbara, CA, USA, 93106

Abstract: Photodetectors and integrated optical receivers operating at 1.55 μm wavelength are crucial for long-haul communication and data transfer system. In this paper, we report the first C-band InAs quantum dash (Qdash) waveguide photodiodes (PDs) with a record-low dark current of 5 pA, a responsivity of 0.26 A/W at 1.55 μm , and open eye diagrams up to 10 Gb/s. These Qdash-based PDs leverage the same epitaxial layers and processing steps as Qdash lasers and can thus be integrated with laser sources for power monitors or amplifiers for pre-amplified receivers, manifesting themselves as a promising alternative to InGaAs and Ge counterparts in low-power optical communication links.

Main Text:

1. Introduction:

Self-assembled quantum-dot (QD) and quantum-dash (Qdash) semiconductor nanostructures have attracted intense interest in optoelectronic devices. Due to the complete carrier confinement and characteristic density of states, dramatically improved device performance have been achieved that is not feasible in conventional quantum-well (QW) structures and bulk materials [1]–[4]. In applications of QD materials, low threshold lasers [5]–[9], high gain optical amplifiers (SOAs) [10], [11], high efficiency solar cells [12] and light-emitting diodes (LEDs) [13] have been reported. The high optical–electrical conversion efficiency from QD photovoltaic cells has spawned intense interest to explore these dense, energetically confined, and spatially isolated nanostructures for use in photodetection devices. Recently, InAs QD waveguide PDs epitaxially grown on (001) Si showed a low dark current of 4.8 nA (dark current density of $4.8 \times 10^{-4} \text{A/cm}^2$) with an internal responsivity of 0.9 A/W in the O-band [14]. Further material quality improvement has led

to a significant reduction in dark current to a value of 0.2 nA biased at -3 V (dark current density of 1.3×10^{-4} A/cm²) for a $3 \times 50 \mu\text{m}^2$ device [15], and to a value of 5.3 pA (dark current density of 3.5×10^{-7} A/cm²) biased at -1 V for a $30 \times 50 \mu\text{m}^2$ device [16]. InAs QD waveguide PDs heterogeneously integrated on Si exhibit dark currents as low as 0.01 nA, together with a responsivity of 0.34 A/W at 1310 nm, a 3 dB bandwidth of 15 GHz, and open-eye diagrams up to 12.5 Gb/s [17]. However, extending the absorption wavelength of these InAs/GaAs QDs based devices to 1.55 μm requires using metamorphic buffers, which typically results in device degradation and lifetime issues [18]. Recent progress in 1.55 μm InAs Qdash material grown on InP substrates has spurred renewed interests in this area [19]. The smaller lattice mismatch (~3%) between InAs/InP and the compressive strain distribution tend to form elongated Qdashes instead of QDs. Injected carriers in the active region are quantum mechanically confined in the localized finite self-assembled wire-like Qdash structures with quasi-zero-dimensions, in a similar way as that in QD structures. Extensive studies have been conducted to explore the inherent inhomogeneous nature and ultra-broad gain profile of Qdash material to make broadband optical amplifiers [19], mode-locked lasers [20], and superluminescent diodes [21] with encouraging results. However, there is no report investigating the Qdash materials for 1.55 μm photodetection to date.

In this paper, we demonstrate 10 Gbit/s non-return-to-zero (NRZ) signal detection by Qdash waveguide PDs in the 1.55 μm telecom window. The InAs Qdash material employed as the absorption region undergoes a growth interruption process to ripen InAs nanostructures for enhanced optical properties [22]. A waveguide p-i-n design with light absorption perpendicular to the current collection was adopted for high-speed, high-efficiency and relatively bias-insensitive operation [23]. The PD operates with an internal quantum efficiency of 29.7 % and a fiber coupled responsivity of 0.26 A/W at a bias voltage of -3 V at 1550 nm and has absorption spectrum covering the whole C-band optical detection window. Due to the isolated carrier confinement in Qdash material as well as the surface passivation of the waveguide PD mesa, a low dark current of 5 pA is achieved for a $30 \times 50 \mu\text{m}^2$ device biased at -1 V. This corresponds to a low dark current density of 3.3×10^{-7} A/cm², which is around five orders of magnitude lower than the state-of-art Ge

PDs [24], and two orders of magnitude lower than commercial InGaAs PDs [25]. Low frequency noise spectroscopy was conducted to identify the generation and recombination related deep levels to obtain a more detailed deep level characterization on the origin of dark currents in these devices. A defect level with an activation energy of 0.2 eV is extracted with a capture cross section of $5.9 \times 10^{-19} \text{cm}^2$. A 3-dB bandwidth of 4.1 GHz was achieved for a narrower mesa waveguide device with a size of $3 \times 30 \mu\text{m}^2$. A 10 Gbit/s eye opening was obtained from the large signal measurement using NRZ signals. This is important since 10 Gb/s Ethernet Passive Optical Networks are becoming the leading technology for 5G mobile networks [26]. The clear eye opening up to a data-rate of 10 Gbit/s manifest a huge potential market for these PDs to be used at a 1.55 μm optical communications system. Finally, based on the defect information and high-speed measurement, the prospect for future material optimization and device design is outlined and a benchmark with state-of-art 1.55 μm p-i-n photodiodes with different materials is presented. In addition, the Qdash PD is made using the same epitaxial layers and fabrication process for a recent 1550 nm Qdash microring laser [27], and can thus be integrated with laser sources for power monitors with significantly simplified process in a fully integrated Qdash transceiver.

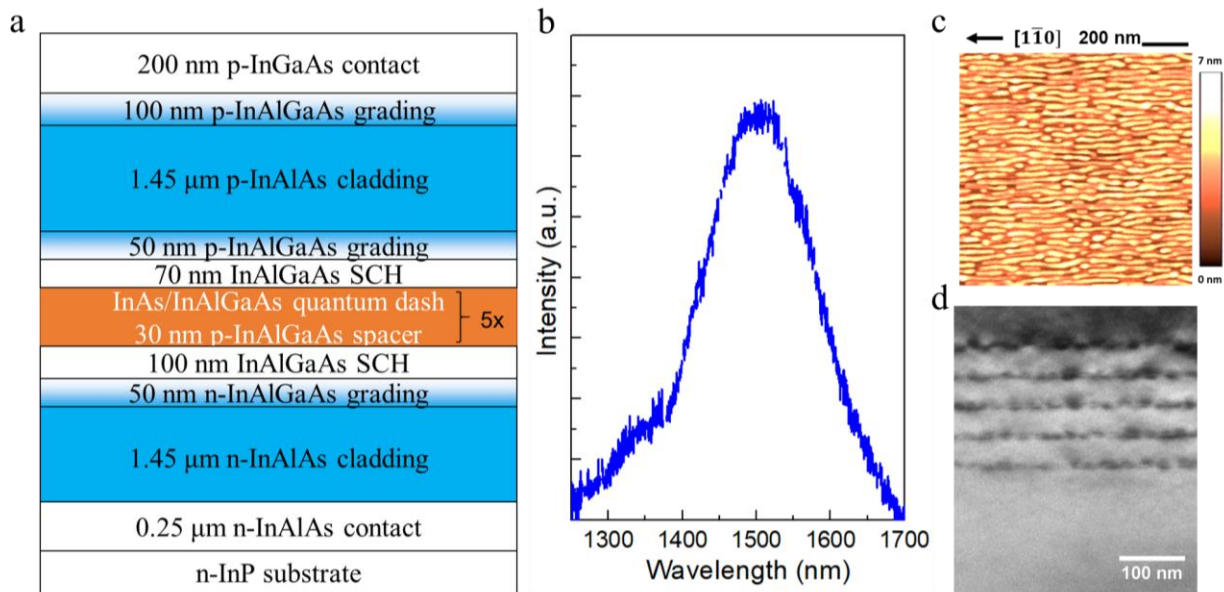


Figure 1. (a) Schematic diagram of the epi structure. (b) Photoluminescence spectrum of the as-grown sample. (c) Atomic force microscopy image of QDashes with a density of $1.3 \times 10^{10} \text{cm}^{-2}$. (d) Cross-sectional transmission electron microscopy image in the QDash active region.

2. Material growth and fabrication:

The epilayer structure of the photodiode is shown in Fig. 1(a). All layers are lattice-matched to InP and are grown on a semi-insulating double-side-polished InP substrate by molecular beam epitaxy (MBE). The epitaxial growth began with a 250 nm *n*-type InAlAs contact layer, a 1.45 μm *n*-type InAlAs cladding layer, a 50 nm InAlGaAs grading layer and 100 nm-thick InAlGaAs digital alloys with alternating lattice-matched InAlAs/InGaAs layers to form a separate-confinement heterostructure (SCH). The absorption layer consists of five Qdash layers that are composed of 3.75 ML InAs grown at 500 °C with 60 sec ripening period under As₂ overpressure. Following the Qdash layer, room-temperature photoluminescence (PL) of the epitaxial layers was conducted with a 671 nm wavelength laser as the excitation source. A ground-state emission at 1500 nm and a full-width-at-half maximum (FWHM) of 98 meV were measured, as shown in Fig. 1(b). The surface morphology of the Qdash material was characterized with atomic force microscopy (AFM), exhibiting elongated dashed along the $[1\bar{1}0]$ direction as shown in Fig. 1(c). A dash density of $1.3 \times 10^{10} \text{ cm}^{-2}$ was obtained. A cross-sectional bright-field transmission electron microscopy (TEM) of the five Qdash layers is presented in Fig. 1(d) under the $\mathbf{g} = (002)$ two-beam condition, which confirms the uniform periodicity of the Qdashes. The growth then proceeded with the *p*-type SCH layer, grading layer, and cladding layer. Finally, a 200-nm-thick *p*-doped InGaAs layer was deposited as the *p*-contact layer.

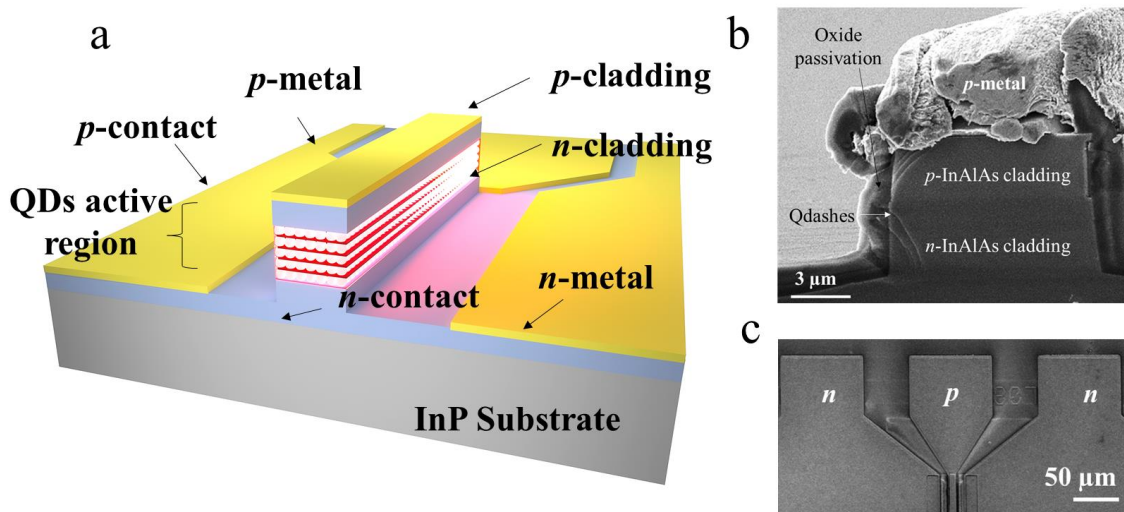


Figure 2. (a) Schematic diagram of the fabricated waveguide photodetector. (b) Top-view and cross-sectional views (c) of the fabricated device.

The as-grown material was then processed into deeply etched rectangular shape waveguides with mesa width ranging from 3 to 50 μm and mesa length ranging from 30 to 300 μm . Inductive coupled plasma etching using Cl_2 , H_2 and Ar with gas flow rates of 6.3, 12.7 and 2 sccm, respectively, were performed at a temperature of 200 $^\circ\text{C}$ and a pressure of 1.4 mTorr. The plasma etching was precisely time-controlled to stop on the n -type InAlAs layer. After etching, the sidewall was passivated with 12 nm of Al_2O_3 by atomic-layer deposition (ALD) followed by a 1- μm -thick SiO_2 layer to suppress the surface leakage current. After contact via opening, Pd/Ti/Pd/Au and Pd/Ge/Pd/Au metal contact stacks were evaporated to form a standard ground-signal-ground (GSG) configuration with a pitch of 150 μm . Finally, facets were cleaved with no additional anti-reflection coatings applied. The full photodetector structure is schematically shown in Fig. 2(a). Cross-sectional view and top-view scanning electron microscope (SEM) images of a fabricated device are shown in Fig. 2(b) and Fig. 2(c), respectively.

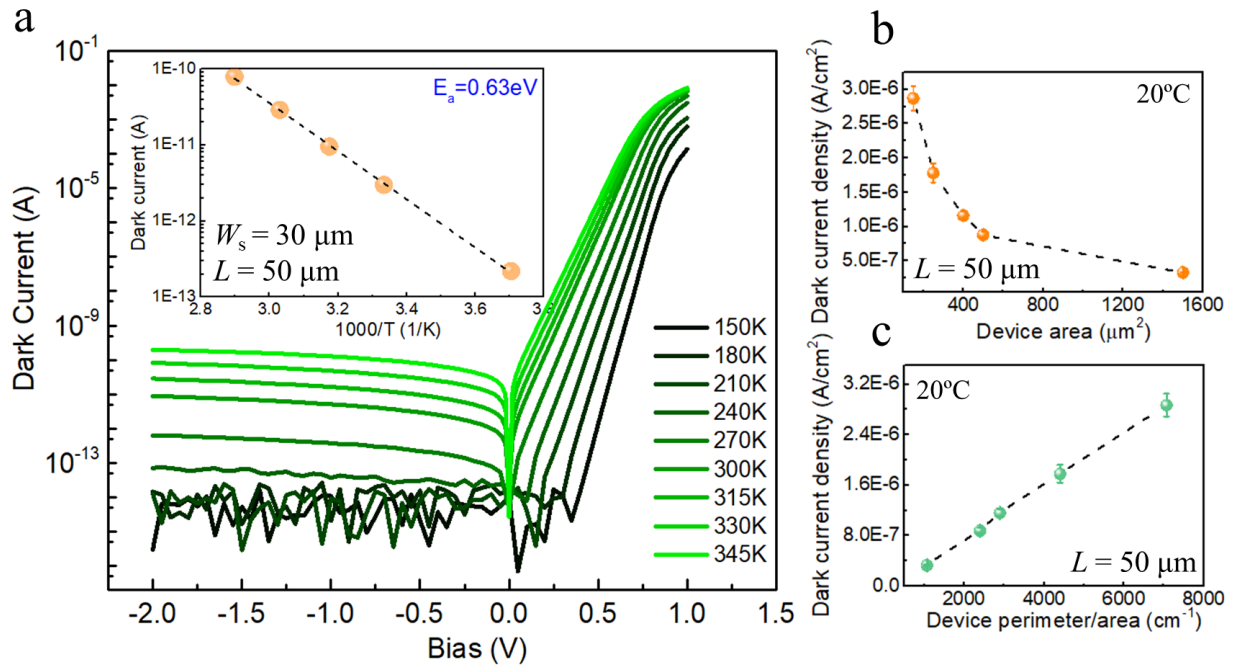


Figure 3. (a) Temperature dependent measurement of the Current-voltage characteristics of a $30 \times 50 \mu\text{m}^2$ device. Inset: Arrhenius plot of temperature dependent dark current at -1 V. Dark current density as a function of (b) the device area and (c) the device perimeter/area for a series of devices with a fixed PD mesa length of 50 μm at room temperature.

3. Measurement and analysis:

The dark current voltage (I-V) curves of a $30 \times 50 \mu\text{m}^2$ photodiode were measured from 150–345 K in a variable temperature probe station and recorded by a semiconductor device analyzer, as shown in Fig. 3(a).

Due to the detection limit, dark currents measured below 240 K are too low to be resolved. At room temperature, a dark current of 5.2 pA is obtained under a bias voltage of -1 V, which corresponds to an ultra-low dark current density of $3.3 \times 10^{-7} \text{ A/cm}^2$. Linear fitting of the Arrhenius plot of the temperature dependent dark current biased at -1 V is shown in the inset in Fig. 3(a). The extracted activation energy (E_a) of 0.63 eV is $\sim 78\%$ of the InAs Qdash bandgap E_g (~ 0.8 eV) at room temperature, indicating that the dark current is dominated by both the diffusion and generation-recombination components. Statistical analysis over a sampling of PDs was performed to reach a fair comparison by taking into account process variations. For a fixed PD mesa length of $50 \mu\text{m}$, dark current and dark current density are plotted as a function of the device area, and device perimeter/area respectively for a series of devices at room temperature. The average dark current density with the narrowest stripes ($2.8 \times 10^{-6} \text{ A/cm}^2$ for $3 \mu\text{m}$ stripes) yielded ~ 8 -fold increase compared to devices with a wide stripe ($3.3 \times 10^{-7} \text{ A/cm}^2$ for $30 \mu\text{m}$ stripes). The slope between the dark current density and device perimeter/area indicates that the surface leakage still exists and requires further improvement of the device passivation process. Still, the dark current density of $3.3 \times 10^{-7} \text{ A/cm}^2$ is around five orders of magnitude lower than the state-of-art Ge PDs [24], and two orders of magnitude lower than the commercial InGaAs PDs [25].

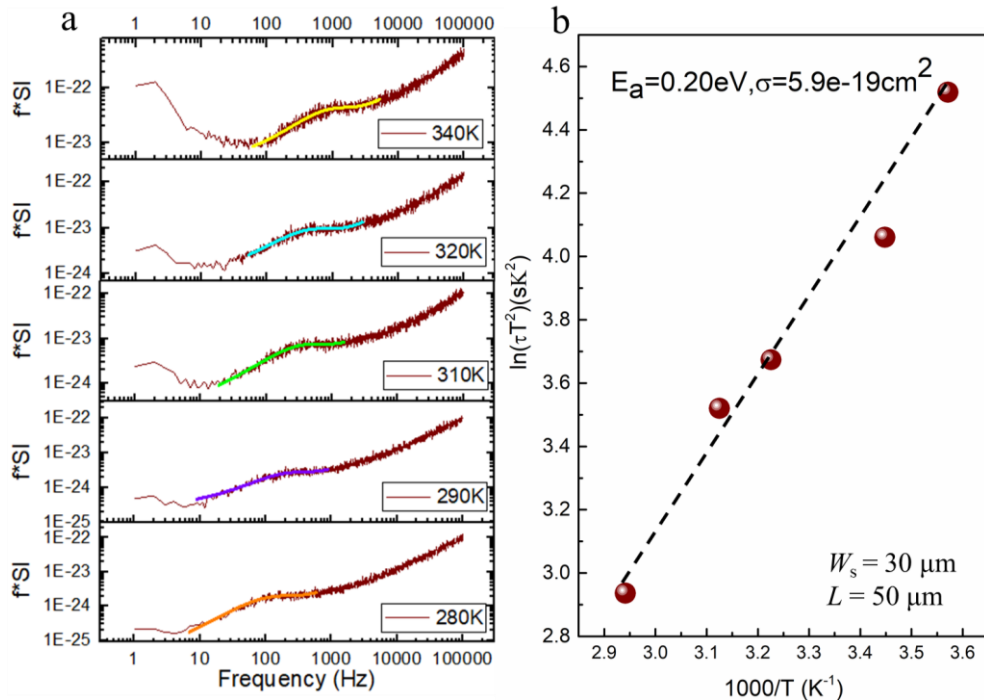


Figure 4. (a) The measured noise spectra under different temperatures with Lorentzian fitting and (b) Arrhenius plot of the deep levels of a $3.0 \times 50 \mu\text{m}^2$ device.

To obtain a more detailed deep level characterization on the origin of dark currents in these devices, low frequency noise spectroscopy (LFNS) measurement was performed over a temperature range from 280-340 K with a step of 10 K and a bias voltage of 300 mV. Details of LFNS measurement are in references [16], [28], [29]. The measured noise spectra are shown in Fig. 4(a). Lorentzian peaks superimposed on the noise spectra corresponds to G-R noise which originates from deep levels in the device. By extracting the time constant by Lorentzian fitting at each temperature, the Arrhenius plot of $\ln(\tau T^2)$ is presented as a function of the reverse of temperature, as shown in Fig. 4(b). A defect level with an activation energy of 0.2 eV is extracted with a capture cross section of $5.9 \times 10^{-19} \text{cm}^2$.

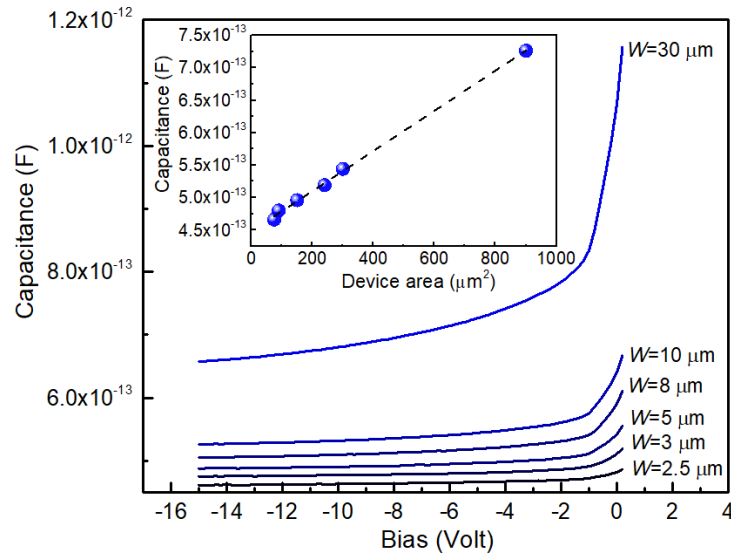


Figure 5. Measured capacitance as a function of reverse bias for a series of devices with a fixed PD mesa length of $30 \mu\text{m}$ and varied PD mesa width at room temperature. Inset: capacitance of the device at -5 V bias. Linear fitting to the data gives rise to a parasitic capacitance of 448 fF .

Fig. 5 shows the capacitance-voltage (C-V) curves for a series of devices with a fixed PD mesa length of $30 \mu\text{m}$ and varied PD mesa width at room temperature. The devices are fully depleted at -2 V and the capacitance biased at -5 V are recorded in the inset of Fig. 5. A linear relationship between the measured capacitance versus device area is expected. The parasitic pad capacitance can be estimated to be 448 fF based on the intercept in the inset of Fig. 5, which is close to the value calculated based on the parallel

plate capacitor model, in which the p -probe pad have an area of around $13500 \mu\text{m}^2$ over a $1\text{-}\mu\text{m}$ -thick SiO_2 layer with a RF dielectric constant of 3.9.

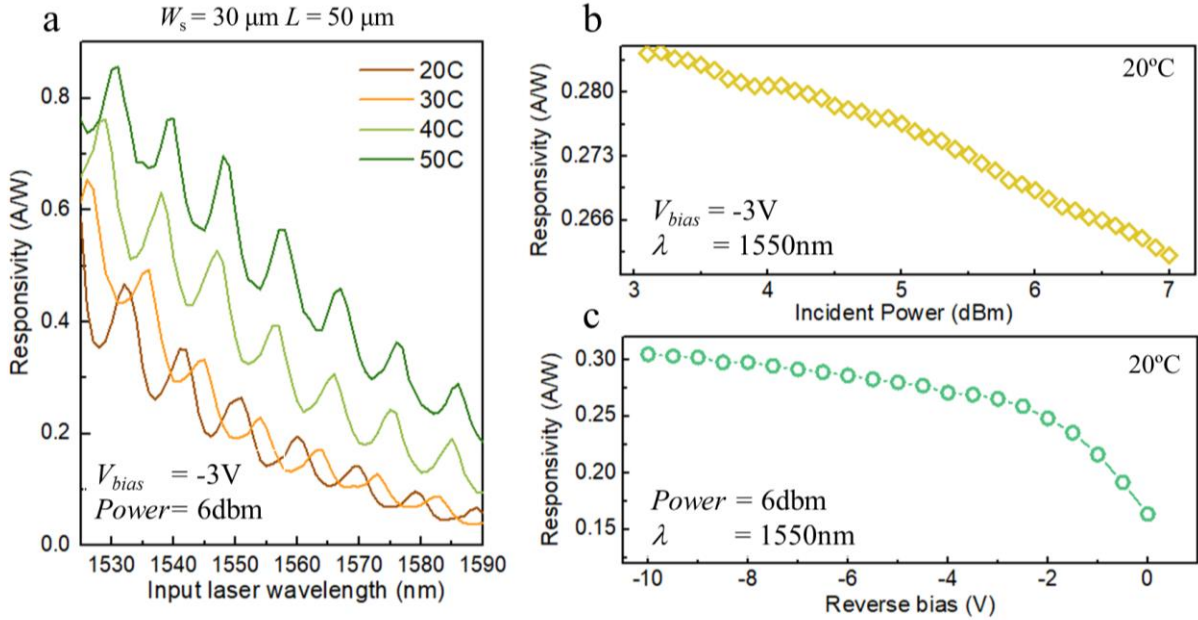


Figure 6. (a) Wavelength dependence of PD internal TE responsivity at various temperatures biased at -3 V . (b) Power dependence of PD responsivity biased at -3 V . (c) Voltage bias dependence of PD responsivity. The device has a size of $3 \times 50 \mu\text{m}^2$.

Optical response of the PDs was measured by coupling light from a tunable laser source to the cleaved facet of PDs by a lensed fiber and adjusting the input polarization by a polarization controller. Fig. 6(a) shows wavelength dependence of the TE responsivity for a $3 \times 50 \mu\text{m}^2$ device. The bias voltage and the input power were fixed at -3 V and 6 dBm , respectively. The coupling loss between the spherical-lensed fiber and the cleaved facet was estimated to be 3 dB . This is obtained by forward biasing a device with the same mesa width but with a longer mesa length as a laser diode, and comparing the measured power from an integrated sphere power meter and a fiber coupled power meter. Improving the optical coupling between fiber and PD facet with a spot size convertor would efficiently increase the responsivity performance [30]. Due to the $\sim 30\%$ reflection at the waveguide facets, Fabry-Perot resonance between the rear and the front facets is observed with oscillatory features superimposed in the responsivity plot. This resonant behavior can be removed by applying antireflection coating on the rear facet. The Qdash layers have a ground state PL peak centered at 1500 nm and the PL intensity drops to 80% and 50% of its maximum value at 1550 nm and 1590 nm respectively. In addition, carriers are generated at lower energy states within the Qdashes

and require more energy to escape at longer wavelengths. Therefore, the responsivity decreases from 0.59 A/W to 0.06 A/W as the input wavelength increases from 1525 nm to 1590 nm. Still, fiber coupled responsivity values in excess of 0.19 A/W were obtained in the 1530-1565 nm spectral range at room temperature. At 1550 nm, the responsivity biased at -3 V increases from 0.26 A/W to 0.67 A/W as the stage temperature increases from 20°C to 50°C. This is because the increase of the temperature redshifts the absorption spectra and reduces the time constant of thermal emission process out of the QDs [31]. At 1550 nm, power dependent response curve and bias dependent response curve are plotted in Fig. 6(b) and Fig. 6(c), respectively. Both a power dependency and a bias dependency are seen in the responsivity. With increased reverse bias, the higher electrical field sweep out the electron and hole pairs within the depletion region more efficiently before they recombine, leading to increased responsivity. The responsivity increased to a maximum value of 0.3 A/W at a bias voltage of -9 V and can be further improved by incorporating a resonant-cavity-enhanced structure with distributed-Bragg mirrors [32]. By adjusting the absorption spectrum of the Qdash layer and the corresponding measurement condition (temperature, bias, etc.), C-band (1530-1565 nm) optical detection is feasible.

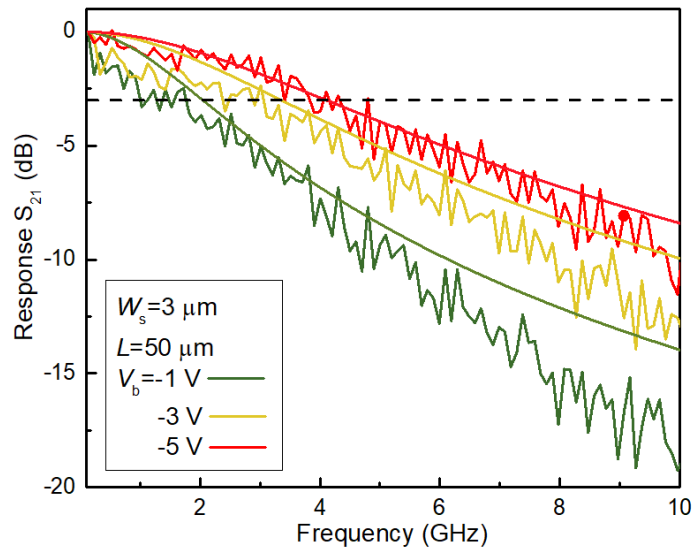


Figure 7. Small-signal frequency responses of $3.0 \times 50 \mu\text{m}^2$ device for various bias voltages.

The small-signal frequency response S_{21} was measured using a lightwave-component analyzer (LCA) with a 1550 nm external laser. The modulated light from the LCA was controlled to be TE light by a polarization controller and input to the PD facet through a spherical lensed fiber. S_{21} characteristics of a 3

$\times 50 \mu\text{m}^2$ device biased at various voltages is presented in Fig. 7. When the voltage bias increases, photogenerated carriers escape from the Qdashes within a shorter period of time, similar to that in InAs/GaAs QDs [33]. This gives rise to a maximum 3dB bandwidth of 4.1 GHz biased at -5 V.

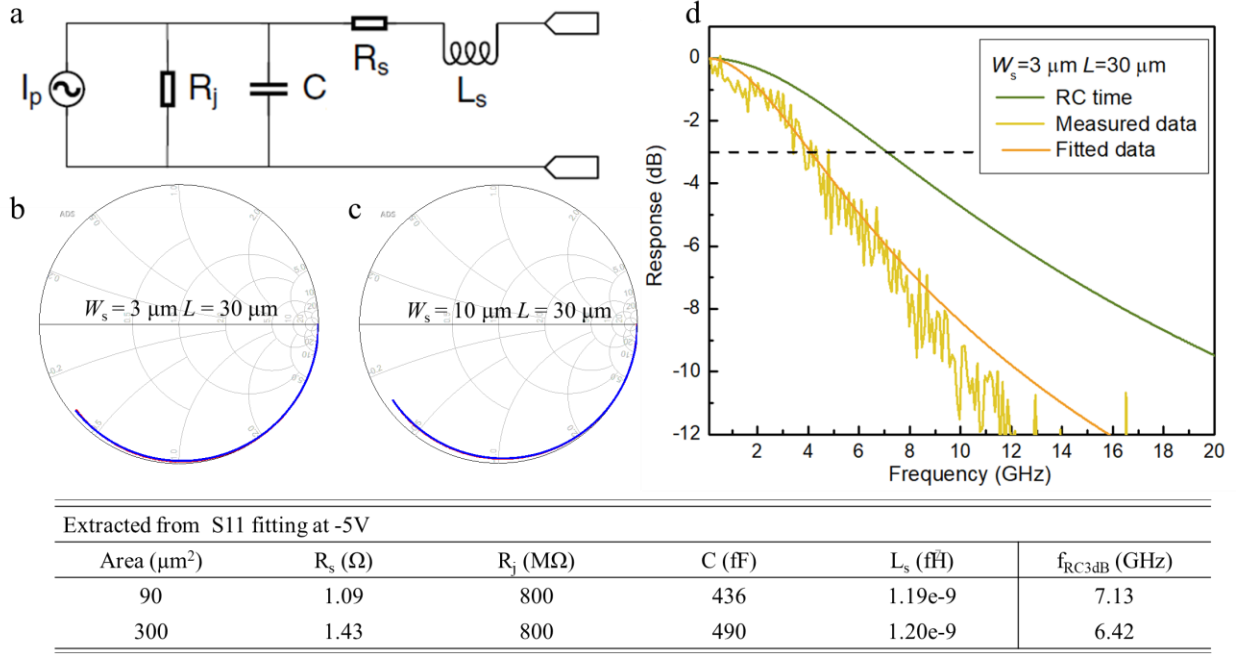


Figure 8 (a) Equivalent circuit model used for the fitting of the Impedance measurement. Measured and fitted curves of reflection S_{11} characteristics for reverse (-5V) biased condition from 0.14 to 20 GHz for (b) a $3.0 \times 30 \mu\text{m}^2$ device and (c) a $10 \times 30 \mu\text{m}^2$ device. (d) A comparison between the calculated RC limit frequency response using the fitting results (green) and the measured small-signal frequency response S_{21} (yellow).

To assess the bandwidth limiting factors, S_{11} characteristics were measured and the parameters were fitted with an equivalent circuit model, as shown in Fig. 8(a). In the model [34], [35], C is the total capacitance, R_s is the series resistance and can be de-embedded from IV characteristics, L_s is the inductance of the probe pads and R_j is the junction resistance. It is noted that the device has a relatively low RC limited bandwidth around 7 GHz, due to the large parasitic capacitance of the contact pad. For the $3.0 \times 30 \mu\text{m}^2$ device, capacitance at -5 V based on the S_{11} measurement is 436 fF , which is also close to the capacitance measured by CV measurement as shown in Fig. 5. Since the capacitance of the device is dominant by the pad capacitance as indicated in the inset of Fig. 5, it is expected that the maximum 3-dB bandwidth could be further improved by reducing the pad capacitance.

Fig. 9 shows the eye diagram of a $3.0 \times 30 \mu\text{m}^2$ photodiode biased at -3 V and operating at a 5 Gbit/s,

7.5 Gbit/s, and 10 Gbit/s data rate. $2^{31}-1$ pseudo-random binary sequence (PRBS) sequences were generated as the data source to drive a lithium-niobate (LN) modulator, which modulates the optical signal coming from a $1.55 \mu\text{m}$ wavelength external tunable laser. The modulated light signal was controlled to be TE light by a polarization controller and was used as an input to the device through a spherical lensed fiber. Clear eye opening up to a data-rate of 10 Gbit/s is observed and manifest that these PDs can be used at a $1.55 \mu\text{m}$ optical communications system

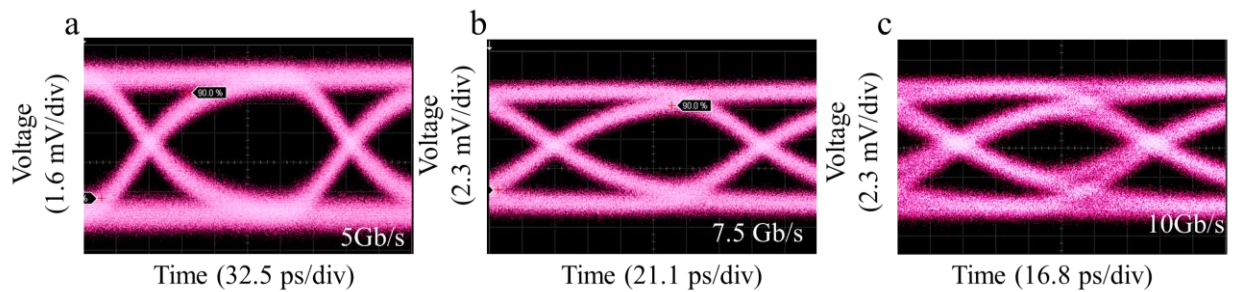


Figure 9. Measured eye diagrams at a bias voltage of -3 V for data-rate ranging from 5 to 10 Gbit/s.

Table 1 summarizes the performance comparison between $1.55 \mu\text{m}$ wavelength p-i-n photodiodes with different platforms or materials. For photodetectors operating at $1.55 \mu\text{m}$ wavelength, most work relied on Ge and bulk III-V semiconductors. Ge detectors possess high bandwidths, high responsivity from visible to near-infrared wavelengths, and are fully compatible with Si complementary metal–oxide–semiconductor (CMOS) manufacturing [24]. More than 70 GHz bandwidth has been reported with an internal responsivity of more than 1 A/W at $1.55 \mu\text{m}$ [36]. However, thermionic emission limits the dark current density in Ge PDs to around $2 - 200 \text{ mA/cm}^2$ at room temperature [36]–[42]. A high dark current density of 0.15 mA cm^{-2} at a reverse bias of -1 V is among the lowest reported value for Ge based PDs [42]. In addition, optical absorption in Ge decreases dramatically at wavelengths beyond $1.55 \mu\text{m}$, excluding them from being used in applications that require wavelengths above $1.57 \mu\text{m}$. Low temperature (LT)-GaAs was also able to absorb long wavelength light signals due to the midgap defects or As precipitates. However, the below band-gap absorption coefficient is much smaller than the normal band-to-band absorption coefficient. The response efficiency of this type of detectors is low even at high reverse bias, especially at or above $1.55 \mu\text{m}$ [43]. InGaAs PDs represent the most competitive candidate for $1.55 \mu\text{m}$ detection. Compared to the

commercial InGaAs PDs [25], the dark current density of the Qdash based PDs reported here is at least two orders of magnitude lower. However, there still remains problems associated with relatively small responsivity and 3-dB bandwidth for the Qdash PDs. Therefore, it is necessary to address the small optical overlap on absorption layers by introducing resonant cavity enhanced structures and increasing the number of Qdash layers, and to improve the optical coupling between fiber and PD facets by incorporating spot size convertor designs. Currently, the relatively large pad capacitance limits the maximum 3-dB bandwidth to a value of 4.1 GHz. A several micron-thick benzocyclobutene (BCB, $\epsilon = 2.6$) layer can be used to planarize the device surface before metal deposition to lower the parasitic capacitance. In addition, the current epitaxial structure is comprised of a ~ 4 μm thick InAlAs/InAlGaAs graded-index separate confinement heterostructure (GRINSCH). The bandwidth can be further improved by engineering the design of the epitaxial layers, reducing the device sizes, and applying traveling wave electrodes to better balance between the bandwidth and the quantum efficiency [44].

TABLE I. Performance comparison among high-speed p-i-n photodiodes.

	Responsivity [A/W]	Dark Current (DC) [nA]	DC density [A/cm ²] (Bias voltage [V])	3dB bandwidth [GHz]	Junction area [μm^2]	Reference
LT-GaAs	7.7×10^{-3}	1.75	3.5×10^{-5} (-4 V)	6	5024	[43]
Ge	1.09	3500	5.5 (-2 V)	42.5	64	[41]
Ge	0.13	93	1.5×10^{-4} (-1 V)	NA	62500	[42]
Ge	1	100	1 (-1 V)	70	10	[36]
GeSn/Ge	0.2	44	4.4×10^{-2} (-1 V)	10	100	[45]
InGaAs/InP	0.45	1.6	3.2×10^{-3} (-4 V)	33	50	[46]
InGaAs/InP	0.8	0.5	5×10^{-5} (-5 V)	9	1017	[25]
InGaAs/GaAs	1.05	1	4.2×10^{-5} (-5 V)	13	2122	[47]
InAs Qdash	0.26	5.2×10^{-3}	3.3×10^{-7} (-3 V)	4.1	150	This work

Conclusions:

In summary, we presented Qdash PDs grown on (001) InP using the same epitaxial layers and fabrication process for a Qdash laser. 10 Gbit/s operation with a fiber coupled responsivity of 0.26 A/W at 1550 nm and a 3-dB bandwidth of 4.1 GHz have been demonstrated. A low dark current density of 3.3×10^{-7} A/cm² has been achieved, which is around five orders of magnitude lower than Ge PDs [24], and two orders of

magnitude lower than commercial InGaAs PDs [25]. In addition, QD material in the 1.3 μm region has high device performance even in the presence of defects introduced by lattice-mismatched III/V-on-Si growth [1]–[4]. InAs QD lasers [5]–[9], amplifiers [10], [11], PDs [16] grown on Si substrates are already showing exceptional performance. The same technology can be synchronously leveraged for 1.55 μm Qdash devices to circumvent crystal defects in heteroepitaxy growth on Si. The parallel efforts in the growth of GaAs-based devices on Si have provided us a lot of insight in managing the lattice and thermal mismatch, as well as defect mitigation for good device performance. The demonstration of high performance 1.3 μm InAs QD lasers, amplifiers, PDs grown on Si substrates proves that these issues are an exercise in engineering, and some of the lessons there can be leveraged: e.g., combining the techniques of strained-layer superlattices (SLSs), thermal cycle annealing, selective patterning for aspect ratio trapping, etc. for defect reduction. With further material, device structure optimization, and the availability of large area blanket InP-on-Si substrate, one can envision the prospects of using Qdash material in future low-power optical communication links and scaling photonic integrated circuits to 300 mm diameter wafer size in high volume applications.

Acknowledgements

This work was funded in part by the Advanced Research Projects Agency-Energy (ARPA-E), U.S. Department of Energy, under Award Number DE-AR0001042, in part by the Shanghai Sailing Program (17YF1429300), in part by the National Key Research and Development Program of China (No. 2018YFB2201000) and in part by ShanghaiTech University startup funding (F-0203-16-002). The views and opinions of authors expressed herein do not necessarily state or reflect those of the United States Government or any agency thereof.

References

- [1] J. C. Norman, D. Jung, Y. Wan, and J. E. Bowers, “Perspective: The future of quantum dot photonic integrated circuits,” *APL Photonics*, vol. 3, no. 3, p. 30901, 2018.
- [2] K. Nishi, K. Takemasa, M. Sugawara, and Y. Arakawa, “Development of Quantum Dot Lasers for Data-Com and Silicon Photonics Applications,” *IEEE J. Sel. Top. Quantum Electron.*, vol. 23, no. 6, pp. 1–7, Nov. 2017.

- [3] D. Bimberg and U. W. Pohl, "Quantum dots: promises and accomplishments," *Mater. Today*, vol. 14, no. 9, pp. 388–397, 2011.
- [4] Y. Wan *et al.*, "Optically pumped 1.3 μm room-temperature InAs quantum-dot micro-disk lasers directly grown on (001) silicon," *Opt. Lett.*, vol. 41, no. 7, pp. 1664–1667, 2016.
- [5] S. Chen *et al.*, "Electrically pumped continuous-wave III–V quantum dot lasers on silicon," *Nat. Photonics*, vol. 10, no. 5, pp. 307–311, May 2016.
- [6] Y. Wan *et al.*, "1.3 μm submilliamp threshold quantum dot micro-lasers on Si," *Optica*, vol. 4, no. 8, pp. 940–944, Aug. 2017.
- [7] D. Jung *et al.*, "High efficiency low threshold current 1.3 μm InAs quantum dot lasers on on-axis (001) GaP/Si," *Appl. Phys. Lett.*, vol. 111, no. 12, p. 122107, Sep. 2017.
- [8] J. Kwoen, B. Jang, K. Watanabe, and Y. Arakawa, *2019 High-temperature continuous-wave operation of directly grown InAs GaAs quantum dot lasers on on-axis Si (001).pdf*, vol. 27, no. 3. Optical Society of America, 2019, p. 2681.
- [9] Y. Wan *et al.*, "Sub-wavelength InAs quantum dot micro-disk lasers epitaxially grown on exact Si (001) substrates," *Appl. Phys. Lett.*, vol. 108, no. 22, p. 221101, 2016.
- [10] S. Liu *et al.*, "High-Performance O-Band Quantum-Dot Semiconductor Optical Amplifiers Directly Grown on a CMOS Compatible Silicon Substrate," *ACS Photonics*, Sep. 2019.
- [11] A. Kotb, K. E. Zoiros, and C. Guo, "2 Tb/s all-optical gates based on two-photon absorption in quantum dot semiconductor optical amplifiers," *Opt. Laser Technol.*, vol. 112, pp. 442–451, Apr. 2019.
- [12] V. Aroutiounian, S. Petrosyan, A. Khachatryan, and K. Touryan, "Quantum dot solar cells," *J. Appl. Phys.*, vol. 89, no. 4, pp. 2268–2271, 2001.
- [13] S. Chen *et al.*, "InAs/GaAs Quantum-Dot Superluminescent Light-Emitting Diode Monolithically Grown on a Si Substrate," *ACS Photonics*, vol. 1, no. 7, pp. 638–642, Jul. 2014.
- [14] Y. Wan *et al.*, "Monolithically integrated InAs/InGaAs quantum dot photodetectors on silicon substrates," *Opt. Express*, vol. 25, no. 22, p. 27715, Oct. 2017.
- [15] D. Inoue *et al.*, "Low-dark current 10 Gbit/s operation of InAs/InGaAs quantum dot p-i-n photodiode grown on on-axis (001) GaP/Si," *Appl. Phys. Lett.*, vol. 113, no. 9, p. 093506, Aug. 2018.
- [16] J. Huang *et al.*, "Defect Characterization of InAs/InGaAs Quantum Dot p-i-n Photodetector Grown on GaAs-on-V-Grooved-Si Substrate," *ACS Photonics*, vol. 6, no. 5, pp. 1100–1105, May 2019.
- [17] B. Tossoun *et al.*, "Indium arsenide quantum dot waveguide photodiodes heterogeneously integrated on silicon," *Optica*, vol. 6, no. 10, p. 1277, Oct. 2019.
- [18] S. Bhowmick, M. Z. Baten, T. Frost, B. S. Ooi, and P. Bhattacharya, "High performance InAs/In_{0.53}Ga_{0.23}Al_{0.24}As/InP quantum dot 1.55 μm tunnel injection laser," *IEEE J. Quantum Electron.*, vol. 50, no. 1, pp. 7–14, Jan. 2014.
- [19] M. Z. M. Khan, T. K. Ng, and B. S. Ooi, "Self-assembled InAs/InP quantum dots and quantum dashes: Material structures and devices," *Prog. Quantum Electron.*, vol. 38, no. 6, pp. 237–313, Nov. 2014.

- [20] V. Panapakkam *et al.*, “Amplitude and phase noise of frequency combs generated by single-section InAs/InP quantum-dash-based passively and actively mode-locked lasers,” *IEEE J. Quantum Electron.*, vol. 52, no. 11, Nov. 2016.
- [21] B. S. Ooi *et al.*, “Quantum Dashes on InP Substrate for Broadband Emitter Applications,” *IEEE J. Sel. Top. Quantum Electron.*, vol. 14, no. 4, pp. 1230–1238, 2008.
- [22] D. Jung, D. J. Ironside, S. R. Bank, A. C. Gossard, and J. E. Bowers, “Effect of growth interruption in 1.55 μm InAs/InAlGaAs quantum dots on InP grown by molecular beam epitaxy,” *J. Appl. Phys.*, vol. 123, no. 20, May 2018.
- [23] J. E. Bowers and C. A. Burrus, “High-Speed Zero-Bias Waveguide Photodetectors,” *Electron. Lett.*, vol. 22, no. 17, pp. 905–906, 1986.
- [24] J. Michel, J. Liu, and L. C. Kimerling, “High-performance Ge-on-Si photodetectors,” *Nat. Photonics*, vol. 4, no. 8, pp. 527–534, Aug. 2010.
- [25] “Semiconductor Engineering .. Silicon Photonics Comes Into Focus.pdf.” .
- [26] I. 802. . E. W. Group, “Industry connections feasibility assessment for the next generation of EPON,” *Berlin, March 2015*, 2015.
- [27] Y. Wan *et al.*, “Low-Threshold Continuous-Wave Operation of Electrically Pumped 1.55 μm InAs Quantum Dash Microring Lasers,” *ACS Photonics*, vol. 6, no. 2, pp. 279–285, Feb. 2019.
- [28] B. K. Jones, “Low-Frequency Noise Spectroscopy,” *IEEE Trans. Electron Devices*, vol. 41, no. 11, pp. 2188–2197, 1994.
- [29] W. Chen, B. Chen, J. Yuan, A. Holmes, and P. Fay, “Bulk and interfacial deep levels observed in In 0.53Ga 0.47As/GaAs 0.5Sb 0.5 multiple quantum well photodiode,” *Appl. Phys. Lett.*, vol. 101, no. 5, Jul. 2012.
- [30] N. Yasuoka *et al.*, “High-efficiency pin photo-diodes with a spot-size converter for 40 Gb/s transmission systems,” in *European Conference on Optical Communication, ECOC*, 2001, vol. 4, pp. 558–559.
- [31] B. Chen and L. H. Archie, “Carrier dynamics in InP-based PIN photodiodes with InGaAs/GaAsSb type-II quantum wells,” *J. Phys. D. Appl. Phys.*, vol. 46, no. 31, Aug. 2013.
- [32] M. S. Unlu, “Resonant cavity enhanced (RCE) photodetectors,” in *Instrumentation in the Aerospace Industry : Proceedings of the International Symposium*, 1998, vol. 44, pp. 479–487.
- [33] W. H. Chang, W. Y. Chen, T. M. Hsu, N. T. Yeh, and J. I. Chyi, “Hole emission processes in InAs/GaAs self-assembled quantum dots,” *Phys. Rev. B - Condens. Matter Mater. Phys.*, vol. 66, no. 19, pp. 1–8, 2002.
- [34] Y. Chen, Z. Xie, J. Huang, Z. Deng, and B. Chen, “High-speed uni-traveling carrier photodiode for 2 μm wavelength application,” *Optica*, vol. 6, no. 7, p. 884, Jul. 2019.
- [35] Z. Xie, Y. Chen, N. Zhang, and B. Chen, “InGaAsP/InP Uni-Traveling-Carrier Photodiode at 1064-nm Wavelength,” *IEEE Photonics Technol. Lett.*, vol. 31, no. 16, pp. 1331–1334, Jul. 2019.
- [36] S. Lischke *et al.*, “High bandwidth, high responsivity waveguide-coupled germanium p-i-n photodiode,” *Opt. Express*, vol. 23, no. 21, p. 27213, Oct. 2015.
- [37] K. Sun and M. C. Gupta, “Pulse laser sulfur-hyperdoping of germanium and high quantum efficiency photodiodes,” *IEEE Photonics J.*, vol. 8, no. 5, Oct. 2016.

- [38] Y. Bao, K. Sun, N. Dhar, and M. C. Gupta, "Germanium p-n junctions by laser doping for photonics/microelectronic devices," *IEEE Photonics Technol. Lett.*, vol. 26, no. 14, pp. 1422–1425, Jul. 2014.
- [39] M. Takenaka, K. Morii, M. Sugiyama, Y. Nakano, and S. Takagi, "Dark current reduction of Ge photodetector by GeO₂ surface passivation and gas-phase doping," *Opt. Express*, vol. 20, no. 8, p. 8718, Apr. 2012.
- [40] H. Chen *et al.*, "Dark current analysis in high-speed germanium p-i-n waveguide photodetectors," *J. Appl. Phys.*, vol. 119, no. 21, Jun. 2016.
- [41] M. M. P. Fard, G. Cowan, and O. Liboiron-Ladouceur, "Responsivity optimization of a high-speed germanium-on-silicon photodetector," *Opt. Express*, vol. 24, no. 24, p. 27738, Nov. 2016.
- [42] S. B. Samavedam, M. T. Currie, T. A. Langdo, and E. A. Fitzgerald, "High-quality germanium photodiodes integrated on silicon substrates using optimized relaxed graded buffers," *Appl. Phys. Lett.*, vol. 73, no. 15, pp. 2125–2127, 1998.
- [43] Q. Han *et al.*, "High-performance 1.55 μm low-temperature-grown GaAs resonant-cavity-enhanced photodetector," *Appl. Phys. Lett.*, vol. 89, no. 13, 2006.
- [44] X. Lin *et al.*, "High performance waveguide uni-travelling carrier photodiode grown by solid source molecular beam epitaxy," Sep. 2019.
- [45] S. Xu *et al.*, "High-speed photo detection at two-micron-wavelength: technology enablement by GeSn/Ge multiple-quantum-well photodiode on 300 mm Si substrate," *Opt. Express*, vol. 27, no. 4, p. 5798, Feb. 2019.
- [46] P. R. A. Binetti *et al.*, "InP/InGaAs photodetector on SOI photonic circuitry," *IEEE Photonics J.*, vol. 2, no. 3, pp. 299–305, 2010.
- [47] S. Q. Liu *et al.*, "High-performance metamorphic InGaAs resonant cavity enhanced photodetector grown on GaAs substrate," *Appl. Phys. Lett.*, vol. 98, no. 20, May 2011.